

Modeling sphere suspension microstructure and stress

J. J. J. Gillissen* and H. J. Wilson

Department of Mathematics, University College London, Gower Street, London, WC1E 6BT, United Kingdom



(Received 11 May 2018; revised manuscript received 16 July 2018; published 27 September 2018)

We develop a model for the microstructure and the stress, in dense suspensions of non-Brownian, perfectly smooth spheres at vanishing particle Reynolds number. These quantities are defined in terms of the second-order moment \mathbf{a} of the distribution function of the orientation unit vector between hydrodynamically interacting particles. We show, from first principles, that the evolution equation of \mathbf{a} contains a source term that accounts for the association and the dissociation of interacting particle pairs. This term provides a microscopic explanation for typical non-Newtonian behavior, observed in experiments in the literature, including normal stress differences in steady shear flow, as well as time-dependent stress after abruptly reversed shear flow and during oscillating shear flow.

DOI: [10.1103/PhysRevE.98.033119](https://doi.org/10.1103/PhysRevE.98.033119)

I. INTRODUCTION

Suspensions of particles occur in paints, toothpastes, inkjet printers, cement, magma, and many other places. In this work we model the stress in a monodisperse suspension of spherical particles, which are assumed massless, non-Brownian, and perfectly smooth. The particle volume fraction is denoted ϕ . The solvent is assumed Newtonian, inertialess, and incompressible and has a viscosity η . The suspension is subjected to a macroscopic (volume averaged) deformation tensor $\mathbf{E} = \frac{1}{2}(\mathbf{L} + \mathbf{L}^T)$, where \mathbf{U} and $\mathbf{L} = \nabla\mathbf{U}^T$ are the volume averaged fluid velocity vector and fluid velocity gradient tensor, respectively.

We define the particle stress $\mathbf{\Sigma}$ as the volume-averaged stress in the suspension, minus the stress in the absence of the particles. Since the hydrodynamic interaction force between perfectly smooth spheres diverges at contact, the particles do not touch each other, i.e., finite gaps remain between them. Under these conditions, the evolution of the suspension microstructure and the associated stress are exclusively governed by the Stokes equations of fluid motion. One important consequence of this condition is that $\mathbf{\Sigma}$ is linear in \mathbf{E} and that there is no shear rate $\dot{\gamma} = \sqrt{2\mathbf{E}:\mathbf{E}}$ dependence in the nondimensional suspension stress tensor $\mathbf{\Sigma}/\eta\dot{\gamma}$, which depends only on the volume fraction ϕ and on the history of the deformation. In reality, these conditions are not met, since real particles have a finite roughness, and real lubrication films cannot decrease below the atomic length scale. Therefore real particles may experience physical contacts and associated contact friction. In addition, there may be interaction forces, other than hydrodynamic, such as electrostatic or van der Waals. The competition between hydrodynamic forces and other interaction forces may give rise to a $\dot{\gamma}$ dependence in $\mathbf{\Sigma}/\eta\dot{\gamma}$. A decreasing $\mathbf{\Sigma}/\eta\dot{\gamma}$ as a function of $\dot{\gamma}$, referred to as “shear thinning,” may result from attractive interaction forces that pull particles together at low $\dot{\gamma}$, while these attractions

are overcome by the hydrodynamic stress at large $\dot{\gamma}$; see, e.g., Ref. [1]. An increasing $\mathbf{\Sigma}/\eta\dot{\gamma}$ as a function of $\dot{\gamma}$, referred to as “shear thickening,” has been explained by repulsive interaction forces [2]. At high shear rates, these repulsions may be overcome, resulting in direct particle contacts and associated contact friction; see, e.g., Refs. [3,4]. Despite the relevance of shear thinning and thickening, we ignore all nonhydrodynamic effects and associated $\dot{\gamma}$ dependencies in this work. Instead, we consider purely hydrodynamic systems of perfectly smooth spheres. Despite its hypothetical nature, it is believed that this approximate system captures the dominant physics, provided the suspension is sufficiently far from the jammed state.

In the literature, the particle stress $\mathbf{\Sigma}$ is usually modeled as

$$\mathbf{\Sigma} = 2\zeta_0\eta\mathbf{E}, \quad (1)$$

where the relative particle viscosity ζ_0 is taken from shear stress measurements in steady shear flow. Equation (1) does not capture the normal stresses, i.e., the diagonal components of $\mathbf{\Sigma}$, in shear flow, which are significant, when $\phi \gtrsim 0.1$ [5–8], nor does it capture transient effects in time-varying flows, such as the abrupt reversal of shear flow [9–13] or the oscillating shear flow [9,14–18]. Upon the abrupt or continuous reversal of shear flow, the suspension microstructure reorganizes, which corresponds to changes in not only the relative magnitude of the eigenvalues, but also in the eigenvectors of the suspension stress tensor $\mathbf{\Sigma}$, neither of which are captured correctly by Eq. (1).

Previous attempts to properly model these effects are based on two equations: one for the evolution of the microstructure \mathbf{a} and one to express $\mathbf{\Sigma}$ in terms of \mathbf{a} . The microstructure \mathbf{a} is usually defined as the second-order moment $\mathbf{a} = \int \Psi \mathbf{r} \mathbf{r} d^3\mathbf{r}$ of the distribution function $\Psi(\mathbf{r})$ of the separation vector \mathbf{r} of the hydrodynamically interacting particles [19–22].

Reference [20] postulates a model for $\mathbf{\Sigma}$ as a polynomial that is first-order in \mathbf{E} and third-order in \mathbf{a} . The equation of motion for \mathbf{a} involves a corotational memory integral of

*jurriaangillissen@gmail.com

the strain-rate history, involving two exponential relaxation modes: a fast mode that captures transient changes in frictional contacts, and a slow mode that captures microstructural reorganization. The model requires the specification of 10 free parameters, which are obtained by fitting the model to experimental data of the stress tensor after the abrupt reversal of shear flow.

Reference [21] postulates a model, where Σ as well as the corotational time derivative of \mathbf{a} are first-order polynomials in both \mathbf{E} and \mathbf{a} . The model requires the specification of 14 free parameters, which are obtained by fitting the model to simulation data for the startup of shear flow.

The models in Refs. [20,21] are empirical, in the sense that their form is dictated by tensor symmetries and invariances, and a multitude of fit parameters are needed to match the model to experimental data, and little can be said about the physical meaning of these parameters.

In this regard Ref. [19] reduces the number of empirical, tuning parameters, at the expense of introducing physical assumptions. These authors approximate the rotation of the particle pair separation vector as that of a dumbbell. The effect of the surrounding particles on the rotating pair is modeled in an *ad hoc* fashion as rotary diffusion. The model contains three free parameters to specify the corresponding anisotropic diffusion tensor. These parameters are tuned by matching the modeled stress tensor to experimental data of steady shear flow.

The models in Refs. [19–21] contain *ad hoc* terms and require the tuning of associated fit parameters with little physical meaning. Therefore, although reproducing experimental data, limited insight can be derived from these models into the dynamics of the microstructure and the link with the suspension stress.

In this work, we aim to improve on these aspects, by deriving, from first principles, a dynamic model for the suspension microstructure and stress that contains two free parameters only. One parameter is a mere stress proportionality constant, while the second parameter accounts for the association and the dissociation of interacting particle pairs. Our aim is to show how this process governs the dynamics of the microstructure, leading to the typical non-Newtonian behavior of particle suspensions, observed in experiments in the literature.

The starting point of the derivation of our model is the Smoluchowski equation for the distribution function $\Psi(\mathbf{r})$ of the separation vector \mathbf{r} . The length of \mathbf{r} is denoted $r = |\mathbf{r}|$. In order to simplify the problem, we divide the \mathbf{r} -space into a near field, $r < r_{\text{threshold}}$, where $\Psi(\mathbf{r})$ depends only on the orientation unit vector \mathbf{p} , and a far field, $r > r_{\text{threshold}}$, where $\Psi(\mathbf{r})$ is isotropic. The main contribution of this work is the identification of the probability flux between the near field and the far field, and the interpretation of this flux as the association and the dissociation of interacting particle pairs. These processes are governed by the rate of fluid deformation \mathbf{E} that pushes particles together and pulls them apart in the compressive and extensional directions of \mathbf{E} , respectively.

The outline of the remainder of the paper is as follows. In Sec. II the model is derived, and in Secs. III and IV, the model is used to interpret available experimental data concerning steady shear flow and time-dependent shear flow, respectively. Conclusions are summarized in Sec. V.

II. MODEL DERIVATION

A. General considerations

The suspension (mixture) stress \mathbf{S} is defined as the (particles and fluid) volume-averaged stress, which for the case of force-free and purely hydrodynamically interacting particles reads [23]

$$\mathbf{S} = 2\eta\mathbf{E} + \Sigma,$$

where η is the solvent viscosity and Σ is the particle contribution to the suspension stress, also referred to as the particle stress. Each particle generates a stresslet, which is the symmetric, first moment of the hydrodynamic force distribution on the particle surface. Summing the stresslets inside an averaging volume V yields

$$\Sigma = \frac{1}{V} \sum_{\alpha} \oint_{S_{\alpha}} \boldsymbol{\sigma} \cdot \mathbf{n}(\mathbf{x} - \mathbf{x}_{\alpha}) d^2\mathbf{x},$$

where S_{α} is the surface of the α th particle, $\boldsymbol{\sigma} = -p\boldsymbol{\delta} + 2\eta\mathbf{e}$ is the local hydrodynamic stress, p is the local fluid pressure, $\mathbf{e} = \frac{1}{2}(\nabla\mathbf{u} + \nabla\mathbf{u}^T)$ is the local fluid rate of strain tensor, \mathbf{u} is the local fluid velocity vector, and \mathbf{n} is the unit vector normal to S_{α} .

In the dilute regime, $\phi \lesssim 10^{-2}$, the flow disturbance (\mathbf{u} , p) generated by particle α is not influenced by a neighboring particle β , and (\mathbf{u} , p , Σ) can be calculated analytically [24]. In nondilute suspensions, $\phi \gtrsim 10^{-2}$; on the other hand, the particle stress Σ can only be obtained numerically, and this computation requires solving the particle trajectories as well. In this regime, one strategy is to approximate (\mathbf{u} , p) on the spheres, using a moment expansion; see, e.g., Ref. [25]. Increasing the particle concentration ϕ requires an increasing number of moments and associated computational effort. Another strategy is to approximate the fluid equations on a three-dimensional Cartesian grid, with a separate account for the forces in the lubrication layers that are thinner than the grid spacing; see, e.g., Ref. [26].

B. Two-body approximation

In this work we focus on the dense regime: $\phi \gtrsim 10^{-1}$. In this regime, the computational problem is less involved than in the “semidilute” regime, $10^{-2} \lesssim \phi \lesssim 10^{-1}$, since the hydrodynamic interactions are dominated by pairwise lubrication forces, and the multibody, far-field interactions may be ignored. In this regard, it is noted that in semidilute systems the multibody, far-field interactions are relatively weak, and the error in using the two-body approximation is therefore small, even under (semi-)dilute conditions.

In the dense regime, the hydrodynamic interaction forces are concentrated in the narrow gaps between the nearly touching particles, and the corresponding particle stress reads

$$\Sigma = \frac{2}{V} \sum_{\alpha > \beta} \oint_{S_{\alpha\beta}} \boldsymbol{\sigma} \cdot \mathbf{n}(\mathbf{x} - \mathbf{x}_{\alpha}) d^2\mathbf{x}.$$

Here $S_{\alpha\beta}$ is the surface of the gap zone between particles α and β , and the factor of two is included to account for the stress on both particles in each pair. Using that for nearly touching spheres $(\mathbf{x} - \mathbf{x}_{\alpha}) \approx \frac{1}{2}(\mathbf{x}_{\beta} - \mathbf{x}_{\alpha}) = \frac{1}{2}\mathbf{r}_{\alpha,\beta}$, and introducing the

interaction force, $\mathbf{F}_{\alpha,\beta} = \oint_{S_{\alpha\beta}} \boldsymbol{\sigma} \cdot \mathbf{n} d^2\mathbf{x}$, one finds the following two-body approximation for the particle stress [27–30]:

$$\boldsymbol{\Sigma} = \frac{1}{V} \sum_{\alpha>\beta} \mathbf{F}_{\alpha,\beta} \mathbf{r}_{\alpha,\beta} = n \langle \mathbf{F} \mathbf{r} \rangle. \quad (2a)$$

Here $n = N/V$ is the particle number density, N is the number of particles inside the averaging volume V , and $\langle \dots \rangle$ is the symmetric average, involving the probability density function $\Psi(\mathbf{r})$ of the separation vector \mathbf{r} between interacting particles. The evolution of Ψ is governed by the Smoluchowski equation for the two-particle configuration space:

$$\partial_t \Psi + \partial_k (\dot{r}_k \Psi) = 0, \quad (2b)$$

where $\partial_k = \partial/\partial r_k$.

The particle stress [Eq. (2a)] is dominated by particle pairs, with small gaps between them, which correspond to separation vectors \mathbf{r} in a spherical, so-called interaction shell: $2a < r < b$. Here $r = |\mathbf{r}|$. The lower boundary, $r = 2a$, is set by the geometrical constraint, while the upper boundary, $r = b$, marks the transition between the dominating interactions and negligible interactions. The average $\langle \dots \rangle$ in Eq. (2a) is therefore written as

$$\langle \dots \rangle = \int_{|\mathbf{r}|=2a}^{|\mathbf{r}|=b} \Psi \dots d^3\mathbf{r}, \quad (2c)$$

and Ψ is normalized, such that $\int_{|\mathbf{r}|=2a}^{|\mathbf{r}|=b} \Psi d^3\mathbf{r}$ equals the average number of interactions per particle. With increasing ϕ , the interaction length b approaches $2a$, and for sufficiently large ϕ , $\mathbf{r} \approx 2a\mathbf{p}$ in the interaction shell, where $\mathbf{p} = \mathbf{r}/r$ is the orientation unit vector.

We will show below that, under these conditions, the particle stress $\boldsymbol{\Sigma}$ depends on the fourth-order orientation moment $\langle \mathbf{p}\mathbf{p}\mathbf{p}\mathbf{p} \rangle$. Following the polymer literature (see, e.g., Ref. [31]), we will formulate an equation of motion for the second-order orientation moment $\langle \mathbf{p}\mathbf{p} \rangle$ and use a closure relation to express $\langle \mathbf{p}\mathbf{p}\mathbf{p}\mathbf{p} \rangle$ in terms of $\langle \mathbf{p}\mathbf{p} \rangle$. The equation of motion for $\langle \mathbf{p}\mathbf{p} \rangle$ is derived by multiplying Eq. (2b) with $\mathbf{p}\mathbf{p}$ and integrating the result over the interaction shell:

$$\int_{|\mathbf{r}|=2a}^{|\mathbf{r}|=b} p_i p_j [\partial_t \Psi + \partial_k (\dot{r}_k \Psi)] d^3\mathbf{r} = 0.$$

Integration by parts gives

$$\begin{aligned} \partial_t \langle p_i p_j \rangle + \int_{|\mathbf{r}|=2a}^{|\mathbf{r}|=b} \partial_k [\Psi p_i p_j \dot{r}_k] d^3\mathbf{r} \\ - \int_{|\mathbf{r}|=2a}^{|\mathbf{r}|=b} \Psi \dot{r}_k \partial_k (p_i p_j) d^3\mathbf{r} = 0. \end{aligned}$$

The first volume integral can be recast into a surface integral using the divergence theorem. The second integral can be rewritten using $\dot{r}_i = \dot{r} p_i + r \dot{p}_i$ and $\partial_j p_i = (\delta_{ij} - p_i p_j)/r$, giving

$$\begin{aligned} \partial_t \langle p_i p_j \rangle + \oint_{|\mathbf{r}|=b} \Psi p_i p_j p_k \dot{r}_k d^2\mathbf{r} \\ - \int_{|\mathbf{r}|=2a}^{|\mathbf{r}|=b} \Psi (\dot{p}_i p_j + p_i \dot{p}_j) d^3\mathbf{r} = 0. \end{aligned} \quad (3)$$

C. Motion of particle pair

In order to proceed, we require an equation of motion for \dot{r}_k . This equation follows from applying a force balance on one particle of an interacting particle pair, which is referred to as the test particle. The force on the test particle is decomposed into two parts, being the hydrodynamic drag force \mathbf{F}^D with the background, and the lubrication force \mathbf{F} with the second particle of the pair. The lubrication force \mathbf{F} is the force that is used in Eq. (2a) to construct the particle stress. The drag force \mathbf{F}^D is expressed as

$$\mathbf{F}^D = \frac{C_1}{2} \eta a (\mathbf{L} \cdot \mathbf{r} - \dot{\mathbf{r}}),$$

where it is recalled that $\mathbf{L} = \nabla \mathbf{U}^T$ is the mixture volume-averaged velocity gradient tensor. Since the solvent is confined between particles, the prefactor C_1 is ϕ -dependent and larger than that for an isolated particle. Here we model this factor using the Richardson and Zaki correlation for sedimenting particles [32]:

$$C_1 = 6\pi(1 - \phi)^{-3}. \quad (4)$$

The pair lubrication force \mathbf{F} is, to leading order, written as

$$\mathbf{F} = -C_2 \eta a \dot{\mathbf{r}} \cdot \mathbf{p}\mathbf{p}, \quad (5)$$

where the prefactor is given by [33]

$$C_2 = \frac{3\pi}{2} \frac{a}{r - 2a}. \quad (6)$$

Taking both contributions together, the force balance of the test particle, $\mathbf{F}^D + \mathbf{F} = \mathbf{0}$, becomes

$$\frac{C_1}{2} (\mathbf{L} \cdot \mathbf{r} - \dot{\mathbf{r}}) - C_2 \dot{\mathbf{r}} \cdot \mathbf{p}\mathbf{p} = \mathbf{0}. \quad (7)$$

Taking the dot product of Eq. (7) with \mathbf{p} and with $(\delta - \mathbf{p}\mathbf{p})$, respectively, gives

$$\dot{\mathbf{r}} \cdot \mathbf{p} = \frac{C_1}{C_1 + 2C_2} \mathbf{L} : \mathbf{r}\mathbf{p}, \quad (8a)$$

and

$$\dot{\mathbf{r}} \cdot (\delta - \mathbf{p}\mathbf{p}) = \mathbf{L} \cdot \mathbf{r} \cdot (\delta - \mathbf{p}\mathbf{p}), \quad (8b)$$

so that

$$\dot{\mathbf{r}} = \frac{C_1}{C_1 + 2C_2} \mathbf{L} : \mathbf{r}\mathbf{p}\mathbf{p} + \mathbf{L} \cdot \mathbf{r} \cdot (\delta - \mathbf{p}\mathbf{p}). \quad (8c)$$

D. Constitutive equations

To compute the particle stress, we combine Eqs. (2a), (5), and (8), where we approximate $\mathbf{r} \approx 2a\mathbf{p}$ and replace the r -dependent, lubrication force, prefactor C_2 by an effective, r -averaged prefactor \tilde{C}_2 :

$$\boldsymbol{\Sigma} = na^3 \eta \frac{4C_1 \tilde{C}_2}{C_1 + 2\tilde{C}_2} \mathbf{E} : \langle \mathbf{p}\mathbf{p}\mathbf{p}\mathbf{p} \rangle. \quad (9)$$

As can be seen in Eq. (9), the particle stress is proportional to the projection of the Newtonian stress $2\eta\mathbf{E}$ onto the particle pair orientation vectors \mathbf{p} , using the fourth-order orientation moment $\langle \mathbf{p}\mathbf{p}\mathbf{p}\mathbf{p} \rangle$.

The orientation moments, $\langle \mathbf{p}\mathbf{p} \rangle$ and $\langle \mathbf{p}\mathbf{p}\mathbf{p}\mathbf{p} \rangle$, also occur in the rheology of anisotropic particles, notably polymers [31],

and the usual practice is to solve an equation for $\langle \mathbf{p}\mathbf{p} \rangle$ and express $\langle \mathbf{p}\mathbf{p}\mathbf{p}\mathbf{p} \rangle$ in terms of $\langle \mathbf{p}\mathbf{p} \rangle$, using a closure model; see, e.g., Ref. [34]. Here we use the linear closure model, which was developed in Ref. [35], which is accurate for microstructures that are relatively close to isotropy:

$$\begin{aligned} \langle p_i p_j p_k p_l \rangle &= -\frac{1}{35} \langle p_m p_m \rangle (\delta_{ij} \delta_{kl} + \delta_{ik} \delta_{jl} + \delta_{il} \delta_{jk}) \\ &+ \frac{1}{7} (\delta_{ij} \langle p_k p_l \rangle + \delta_{ik} \langle p_j p_l \rangle + \delta_{il} \langle p_j p_k \rangle \\ &+ \langle p_i p_j \rangle \delta_{kl} + \langle p_i p_k \rangle \delta_{jl} + \langle p_i p_l \rangle \delta_{jk}), \end{aligned}$$

where it is noted that the trace $\langle p_m p_m \rangle$ varies, due to a varying number of interactions per particle.

In order to derive an equation of motion for $\langle \mathbf{p}\mathbf{p} \rangle$, we combine Eqs. (2c), (3), and (8), where again we approximate $\mathbf{r} \approx 2a\mathbf{p}$, and we replace C_2 by \tilde{C}_2 :

$$\begin{aligned} \partial_t \langle \mathbf{p}\mathbf{p} \rangle &= \mathbf{L} \cdot \langle \mathbf{p}\mathbf{p} \rangle + \langle \mathbf{p}\mathbf{p} \rangle \cdot \mathbf{L}^T - 2\mathbf{L} : \langle \mathbf{p}\mathbf{p}\mathbf{p}\mathbf{p} \rangle \\ &- \frac{C_1}{C_1 + 2\tilde{C}_2} 2a\mathbf{E} : \oint_{|r|=b} \Psi \mathbf{p}\mathbf{p}\mathbf{p}\mathbf{p} d^2\mathbf{r}. \end{aligned} \quad (10a)$$

The boundary surface integral [final term on the right-hand side of Eq. (10a)] corresponds to an orientation probability flux between the interaction shell and the outer shell. This flux is carried by the rate of strain tensor, $\mathbf{E} = \mathbf{E}^c + \mathbf{E}^e$, which is decomposed into a compressive, inward flow \mathbf{E}^c and an extensional, outward flow \mathbf{E}^e , corresponding to negative and positive eigenvalues of \mathbf{E} , respectively. Since \mathbf{E}^c carries orientation probability from the outer shell to the interaction shell, and \mathbf{E}^e carries orientation probability from the interaction shell to the outer shell, the surface integral in Eq. (10a) is written as

$$\begin{aligned} \mathbf{E} : \oint_{|r|=b} \Psi \mathbf{p}\mathbf{p}\mathbf{p}\mathbf{p} d^2\mathbf{r} \\ &= \mathbf{E}^e : \oint_{|r|=b} \Psi^{\text{inner}} \mathbf{p}\mathbf{p}\mathbf{p}\mathbf{p} d^2\mathbf{r} \\ &+ \mathbf{E}^c : \oint_{|r|=b} \Psi^{\text{outer}} \mathbf{p}\mathbf{p}\mathbf{p}\mathbf{p} d^2\mathbf{r}, \end{aligned} \quad (10b)$$

where Ψ^{inner} and Ψ^{outer} are equal to Ψ , evaluated in the interaction shell and in the outer shell, respectively. To proceed, we make two assumptions. First, since the interaction shell is relatively thin, we assume that Ψ^{inner} is independent of r . Second, since in the outer shell the interparticle distances are relatively large, Ψ^{outer} is assumed to be independent of r and \mathbf{p} , i.e., a constant. Since the integrand is independent of r , and the interaction shell is relatively thin, $(b - 2a)/(2a) \ll 1$, we can use that

$$\oint_{|r|=b} \dots d^2\mathbf{r} \approx (b - 2a)^{-1} \int_{|r|=2a}^{|r|=b} \dots d^3\mathbf{r},$$

and recast the first integral on the right-hand side of Eq. (10b) into a volume integral $\langle \dots \rangle$ as defined in Eq. (2c):

$$\oint_{|r|=b} \Psi^{\text{inner}} \mathbf{p}\mathbf{p}\mathbf{p}\mathbf{p} d^2\mathbf{r} = (b - 2a)^{-1} \langle \mathbf{p}\mathbf{p}\mathbf{p}\mathbf{p} \rangle. \quad (10c)$$

Equation (10b) contains Ψ^{outer} , which is assumed a constant. The value of this constant can be arbitrarily chosen, as it

will be absorbed in one of the two tuning parameters of the model; see Sec. II E. Here we choose $\Psi^{\text{outer}} = [4\pi b^2(b - 2a)]^{-1}$, such that the second integral on the right-hand side of Eq. (10b) becomes

$$\begin{aligned} \oint_{|r|=b} \Psi^{\text{outer}} \mathbf{p}\mathbf{p}\mathbf{p}\mathbf{p} d^2\mathbf{r} \\ &= (b - 2a)^{-1} \oint_{|p|=1} (4\pi)^{-1} \mathbf{p}\mathbf{p}\mathbf{p}\mathbf{p} d^2\mathbf{p}, \end{aligned} \quad (10d)$$

where the fourth-order orientation moment of the isotropic distribution reads [35]

$$\oint_{|p|=1} (4\pi)^{-1} p_i p_j p_k p_l d^2\mathbf{p} = \frac{1}{15} (\delta_{ij} \delta_{kl} + \delta_{ik} \delta_{jl} + \delta_{il} \delta_{jk}). \quad (10e)$$

By combining Eq. (10), we finally arrive at the following microstructure evolution equation:

$$\begin{aligned} \partial_t \langle \mathbf{p}\mathbf{p} \rangle &= \mathbf{L} \cdot \langle \mathbf{p}\mathbf{p} \rangle + \langle \mathbf{p}\mathbf{p} \rangle \cdot \mathbf{L}^T - 2\mathbf{L} : \langle \mathbf{p}\mathbf{p}\mathbf{p}\mathbf{p} \rangle \\ &- \frac{C_1}{C_1 + 2\tilde{C}_2} \frac{2a}{b - 2a} \left\{ \mathbf{E}^e : \langle \mathbf{p}\mathbf{p}\mathbf{p}\mathbf{p} \rangle + \frac{1}{15} [2\mathbf{E}^c + \text{Tr}(\mathbf{E}^c)\delta] \right\}. \end{aligned} \quad (11)$$

The first line of Eq. (11) describes that the \mathbf{p} vectors are rotated by the velocity gradient \mathbf{L} , similarly as material lines. Unlike material lines however, the length of the \mathbf{p} vectors is conserved, and the $2\mathbf{L} : \langle \mathbf{p}\mathbf{p}\mathbf{p}\mathbf{p} \rangle$ term ensures this.

The second line of Eq. (11) represents the flux of orientation probability between the interaction shell and the outer shell. This term corresponds to the association and the dissociation of interacting particle pairs, by the action of fluid deformation, that pushes particles together and pulls them apart in the compressive and extensional directions of \mathbf{E} , respectively.

It is noted, that our model [Eqs. (9) and (11)] can be interpreted as an extension of the model of Ref. [19]. The affine motion [first line of Eq. (11)] is identical to that in Ref. [19], while the second line of Eq. (11) differs from Ref. [19], which modeled this term *ad hoc* as rotary diffusion.

E. Summary

The stress Σ induced by the particles is modeled as

$$\Sigma = \alpha \eta \mathbf{E} : \langle \mathbf{p}\mathbf{p}\mathbf{p}\mathbf{p} \rangle, \quad (12a)$$

where the prefactor is referred to as the ‘‘stress magnitude’’, $\alpha = na^3 4C_1 \tilde{C}_2 / (C_1 + 2\tilde{C}_2)$, which involves the particle drag coefficient C_1 in a particle swarm [see Eq. (4) and Ref. [32]] and the prefactor C_2 of the leading order term of the interparticle lubrication force; see Eq. (6) and Ref. [33]. Equation (12a) involves the fourth-order orientation moment $\langle \mathbf{p}\mathbf{p}\mathbf{p}\mathbf{p} \rangle$ of the distribution function Ψ of the separation vector of interacting particle pairs, where the average $\langle \dots \rangle$ is given by Eq. (2c). In Eq. (12a), $\mathbf{E} = \frac{1}{2}(\mathbf{L} + \mathbf{L}^T)$, $\mathbf{L} = \nabla \mathbf{U}^T$, and \mathbf{U} are the spatially averaged rate of strain tensor, the velocity gradient tensor, and the velocity vector, respectively. The second-order orientation moment is referred to as the microstructure tensor:

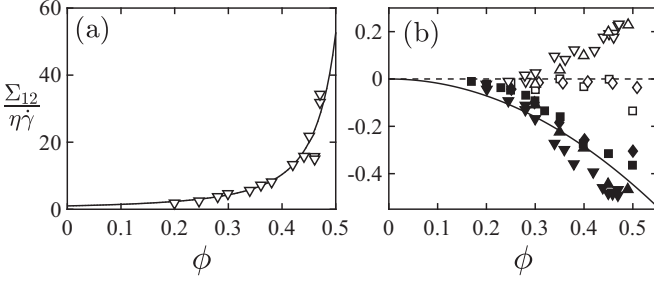


FIG. 1. (a) Measured, steady, relative, shear viscosity: $\zeta_0 = \Sigma_{12}/\eta\dot{\gamma}$, as a function of the particle volume fraction ϕ . Data are taken from Ref. [8]. The line is Eq. (13a), using $\phi_m = 0.58$. (b) Measured, steady, relative, normal stress differences: $\zeta_1 = (\Sigma_{11} - \Sigma_{22})/\Sigma_{12}$ (open markers) and $\zeta_2 = (\Sigma_{22} - \Sigma_{33})/\Sigma_{12}$ (filled markers), as functions of ϕ . Δ , \blacktriangle : $a = 20 \mu\text{m}$ [8]; ∇ , \blacktriangledown : $a = 70 \mu\text{m}$ [8]; \square , \blacksquare : $a = 35 \mu\text{m}$ [7]; \diamond , \blacklozenge : $a = 70 \mu\text{m}$ [7]. The solid line is Eq. (13b) using $\phi_m = 0.58$. The dashed line is $\zeta_1 = 0$.

$\langle \mathbf{p}\mathbf{p} \rangle = \mathbf{a}$, whose evolution is modeled as

$$\partial_t \langle \mathbf{p}\mathbf{p} \rangle = \mathbf{L} \cdot \langle \mathbf{p}\mathbf{p} \rangle + \langle \mathbf{p}\mathbf{p} \rangle \cdot \mathbf{L}^T - 2\mathbf{L} : \langle \mathbf{p}\mathbf{p}\mathbf{p}\mathbf{p} \rangle - \beta \{ \mathbf{E}^e : \langle \mathbf{p}\mathbf{p}\mathbf{p}\mathbf{p} \rangle + \frac{1}{15} [2\mathbf{E}^c + \text{Tr}(\mathbf{E}^c)\delta] \}, \quad (12b)$$

where the prefactor is referred to as the ‘‘microstructure parameter’’, $\beta = [C_1/(C_1 + 2\tilde{C}_2)][2a/(b - 2a)]$, which controls the rate of particle pair association and dissociation. Tensors \mathbf{E}^c and \mathbf{E}^e are the compressive (negative eigenvalues) and the extensional (positive eigenvalues) parts of \mathbf{E} .

In the following section, we specify the free parameters α and β , by matching the numerical solution of Eq. (12) to experimental data from the literature, regarding the shear and normal stresses in steady shear flow.

III. STEADY SHEAR FLOW

Defining 1, 2, and 3 as the flow direction, the gradient direction and the vorticity direction, respectively, the velocity gradient tensor in steady shear flow is given by $\mathbf{L} = \dot{\gamma}\delta_1\delta_2$, where the shear rate is defined as $\dot{\gamma} = \sqrt{2\mathbf{E} : \mathbf{E}}$. The particle stress tensor Σ in steady shear flow is characterized by three dimensionless parameters: the relative shear viscosity, $\zeta_0 = \Sigma_{12}/(\eta\dot{\gamma})$, and the first and second, relative, normal stress differences, $\zeta_1 = (\Sigma_{11} - \Sigma_{22})/\Sigma_{12}$ and $\zeta_2 = (\Sigma_{22} - \Sigma_{33})/\Sigma_{12}$. Figure 1 shows experimental data for ζ_0 , ζ_1 , and ζ_2 as functions of the particle volume fraction ϕ . Figure 1(a) shows that with increasing ϕ , the shear viscosity ζ_0 diverges, which is modeled with the Krieger-Dougherty equation [36]:

$$\zeta_0 = \left(1 - \frac{\phi}{\phi_m}\right)^{-2}. \quad (13a)$$

Here ϕ_m is the maximum packing volume fraction, which for the data in Fig. 1(a) takes the value of $\phi = 0.58$.

As illustrated in Fig. 1(b), it is generally observed that $\zeta_2 < 0$, and the relation between ζ_2 and ϕ is modeled as

$$\zeta_2 = -0.6 \left(\frac{\phi}{\phi_m}\right)^2. \quad (13b)$$

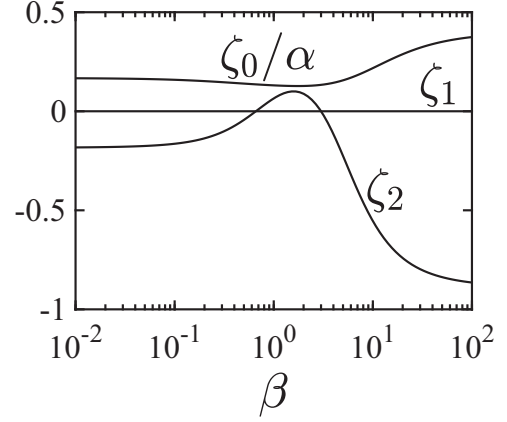


FIG. 2. Modeled [Eq. (12)], steady, relative, shear viscosity $\zeta_0/\alpha = \Sigma_{12}/(\alpha\eta\dot{\gamma})$ and relative, normal stress differences: $\zeta_1 = (\Sigma_{11} - \Sigma_{22})/\Sigma_{12}$ and $\zeta_2 = (\Sigma_{22} - \Sigma_{33})/\Sigma_{12}$ as functions of the microstructure parameter β .

The magnitude and sign of ζ_1 , however, depend on additional details. In shear-invariant suspensions, ζ_1 is usually observed to be relatively small and negative, $|\zeta_1| \ll |\zeta_2|$ [5–7,37–39], while in strongly shear thickening suspensions ζ_1 has been found to be relatively large and positive [37–39]. It is therefore believed that ζ_1 depends on the nature of the interaction force, where $|\zeta_1| \ll |\zeta_2|$ and $\zeta_1 \sim |\zeta_2|$ correspond to relatively weak and relatively strong contact forces, respectively. The focus of the present paper is on contactless particles, i.e., $|\zeta_1| \ll |\zeta_2|$.

Both observations of a negative ζ_2 and a relatively small ζ_1 follow from our model [Eq. (12)]. Assuming $\beta \gg 1$, Eq. (12b) predicts a perfect alignment of the pair interaction vector with the compressive axis of the rate of strain tensor, i.e., $\mathbf{p} = (-1, 1, 0)/\sqrt{2}$. Using that $\mathbf{a} = \mathbf{p}\mathbf{p}$, and that $\Sigma = \alpha\eta\mathbf{E} : \mathbf{a}\mathbf{a}$, we find the following stress tensor:

$$\Sigma = \frac{\alpha\eta\dot{\gamma}}{2} \begin{pmatrix} -1 & 1 & 0 \\ 1 & -1 & 0 \\ 0 & 0 & 0 \end{pmatrix}, \quad (14)$$

which corresponds to relative normal stress differences of $\zeta_1 = (\Sigma_{11} - \Sigma_{22})/\Sigma_{12} = 0$ and $\zeta_2 = (\Sigma_{22} - \Sigma_{33})/\Sigma_{12} = -1$, in qualitative agreement with the experimental data in Fig. 1(b).

Next we numerically compute the steady solution to Eq. (12). Figure 2 shows the resulting relative, shear viscosity, $\zeta_0/\alpha = \Sigma_{12}/(\alpha\eta\dot{\gamma})$, and relative normal stress differences ζ_1 and ζ_2 as functions of the microstructure parameter β . Note that steady stress ratios, such as ζ_0/α , ζ_1 , and ζ_2 , do not depend on the stress magnitude α .

Figure 2 shows that the modeled relative, first normal stress difference $\zeta_1(\beta) = 0$, which is consistent with contactless systems, as discussed above. The behavior of $\zeta_2(\beta)$, on the other hand, is nontrivial. For $\beta < 3$, $\zeta_2(\beta)$ shows unphysical, nonmonotonic, and positive behavior. At $\beta = 3$, the modeled system is Newtonian, i.e., $\zeta_1 = \zeta_2 = 0$. For $\beta > 3$, $\zeta_2(\beta)$ is monotonically decreasing to its saturation value, $\zeta_2 \approx -0.9$. The modeled $\zeta_2(\beta)$ relation is reasonably well captured by $\zeta_2 = -0.6 \arctan[(\beta - 3)/5]$. In the literature, the relation

between ζ_2 and ϕ is usually modeled with Eq. (13b). Our model [Eq. (12)] therefore reproduces Eq. (13b), by choosing

$$\beta = 3 + 5 \tan \left[\left(\frac{\phi}{\phi_m} \right)^2 \right]. \quad (15a)$$

Figure 2 shows the modeled, relative, shear viscosity ζ_0/α as a function of β . In the region of interest, $\beta \geq 3$, the data are reasonably well captured by, $\zeta_0/\alpha = 0.12 + 0.17 \arctan [(\beta - 3)/10]$. In the literature, the relation between ζ_0 and ϕ is usually modeled with Eq. (13a). Our model [Eq. (12)] therefore reproduces Eq. (13a), by choosing

$$\alpha = \left(1 - \frac{\phi}{\phi_m} \right)^{-2} \left[0.12 + 0.09 \left(\frac{\phi}{\phi_m} \right)^2 \right]^{-1}. \quad (15b)$$

In summary, by choosing α and β according to Eq. (15), the model [Eq. (12)] reproduces the volume fraction dependence of the suspension shear viscosity, referred to as the Krieger-Dougherty equation [Eq. (13a) and Fig. 1(a)], as well as that of the first and second normal stress differences [Eq. (13b) and Fig. 1(b)].

IV. TRANSIENT SHEAR FLOW

A. Shear reversal

We use Eq. (12) to compute the time-dependent microstructure \mathbf{a} and the particle stress Σ after shear reversal. To this end, we use the Euler forward, time integration scheme and a time step of $\Delta t = 0.01/\dot{\gamma}$. The initial conditions for the microstructure are isotropic, $\mathbf{a} = \delta/3$, and the microstructure parameter is $\beta = 6$. In the simulation, the suspension is sheared until a steady state is reached, after which the shear direction is reversed. The reversal induces a reorganisation of the microstructure and the attainment of a new steady state. The resulting time-dependent microstructure and particle stress tensor are shown in Figs. 3(a) and 3(b). In those figures, the flow direction is switched from negative to positive at $t = 0$.

To explain these results, we note that for $\beta \gg 1$, Eq. (12) predicts that the microstructure \mathbf{a} aligns with the compressive axis of the rate of strain tensor \mathbf{E} and that $\Sigma \sim \mathbf{E} : \mathbf{a}\mathbf{a}$. In Eq. (16) below we sketch the evolution of the respective tensors, \mathbf{E} , \mathbf{a} , and Σ , before, and after shear reversal, where, for clarity, we omit the numerical prefactors and consider only the dominant components, in the flow and gradient directions. In this simplified notation, before shear reversal, the tensors take the following form:

$$\mathbf{E} \sim \begin{pmatrix} 0 & -1 \\ -1 & 0 \end{pmatrix}, \quad \mathbf{a} \sim \begin{pmatrix} 1 & 1 \\ 1 & 1 \end{pmatrix}, \quad \Sigma \sim \begin{pmatrix} -1 & -1 \\ -1 & -1 \end{pmatrix}. \quad (16a)$$

Right after reversal, \mathbf{a} is aligned with the extensional axis of the reversed \mathbf{E} :

$$\mathbf{E} \sim \begin{pmatrix} 0 & 1 \\ 1 & 0 \end{pmatrix}, \quad \mathbf{a} \sim \begin{pmatrix} 1 & 1 \\ 1 & 1 \end{pmatrix}, \quad \Sigma \sim \begin{pmatrix} 1 & 1 \\ 1 & 1 \end{pmatrix}. \quad (16b)$$

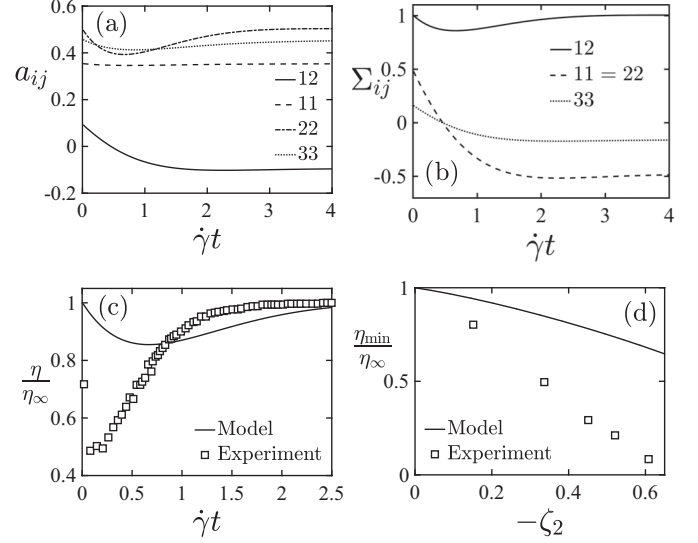


FIG. 3. Modeled [Eq. (12)] time-dependent components of (a) the microstructure \mathbf{a} and (b) the particle stress Σ after shear reversal, using $\beta = 6$. (c) Modeled time-dependent particle viscosity: $\eta = \Sigma_{12}/\dot{\gamma}$, scaled with the steady value η_∞ , together with experimental data, which were taken at a volume fraction of $\phi = 0.4$, and a maximum packing volume fraction [defined in Eq. (13a)] of $\phi_m = 0.54$ [12]. (d) Modeled minimum particle viscosity: η_{\min} [minimum of curve in (c)], after shear reversal, scaled by the steady value η_∞ , using various $\beta \in [3, 11]$, corresponding to various ζ_2 (see Fig. 2), together with experimental data, with varying volume fractions $\phi \in [0.3, 0.5]$ [12], where ζ_2 is estimated using Eq. (13b).

Then, as governed by Eq. (12), the microstructure \mathbf{a} realigns to the compressive axis of \mathbf{E} :

$$\mathbf{E} \sim \begin{pmatrix} 0 & 1 \\ 1 & 0 \end{pmatrix}, \quad \mathbf{a} \sim \begin{pmatrix} 1 & -1 \\ -1 & 1 \end{pmatrix}, \quad \Sigma \sim \begin{pmatrix} -1 & 1 \\ 1 & -1 \end{pmatrix}. \quad (16c)$$

Equation (16) illustrates that, in equilibrium, particle pairs align in the compressive direction, and right after shear reversal, they are aligned in the extensional direction, which corresponds to positive normal stresses. Since this configuration is unstable, the system reorganizes to an equilibrium with pair orientations in the compressive direction, which corresponds to negative normal stresses. These changes in the sign of the normal stresses are in qualitative agreement with experimental data [10,11].

During the reorganization of the microstructure, the dissociation of interacting particle pairs precedes the association, which is reflected by the shear stress passing through a minimum, as seen in Fig. 3(b). This transient behavior is also in qualitative agreement with experimental data [9–13].

In Fig. 3(c) the model predictions are compared to the data of Ref. [12], which were taken at a volume fraction of $\phi = 0.4$, and a maximum volume fraction [defined in Eq. (13a)] of $\phi_m = 0.54$. According to Eq. (15a), these values correspond to $\beta = 6$, which is used in the corresponding computations. As seen in Fig. 3(c), the computational results agree qualitatively with the experimental data, both showing a decrease and a subsequent recovery of the shear stress after flow reversal.

In Fig. 3(d) we consider the stress minimum, scaled with the steady value $\eta_{\min}/\eta_{\infty}$, as a function of the steady, relative, second normal stress difference ζ_2 . The subscript ∞ denotes that the quantity is measured at steady state, i.e., at infinite time after shear reversal. In the computations, we vary ζ_2 by varying the microstructure parameter β (see Fig. 2). The computational results are plotted (line) together with the experimental data (markers), which were taken at various volume fractions: $\phi \in [0.3, 0.5]$ [12]. The experimental ζ_2 is estimated using Eq. (13b). Again there is qualitative agreement between model and experiment, both showing a (nearly) linear decrease in $\eta_{\min}/\eta_{\infty}$ versus ζ_2 . This agreement supports that the model captures the correct qualitative dynamics of the microstructure.

Quantitatively, however, the measured stress decrease is sharper, and a few fold larger than the one computed; see Figs. 3(c) and 3(d). In the literature, the sharp stress decrease has been attributed to physical contacts between particles [13]. When the shear stress is reversed, the associated contact forces relax almost instantaneously. In the present model we do not capture such effects, since the particles are assumed perfectly smooth, and the associated interactions are purely hydrodynamic and without physical contact.

B. Oscillating shear stress

We use Eq. (12) to compute the time-dependent microstructure \mathbf{a} and the particle stress Σ in oscillating shear flow. In this flow, the shear rate is given by $\dot{\gamma} = \dot{\gamma}_0 \cos(\omega t)$, where $\dot{\gamma}_0$ is the shear rate amplitude and ω is the angular oscillation frequency. Simulations of Eq. (12) are conducted for various strain amplitudes, $\gamma_0 = \dot{\gamma}_0/\omega$, ranging between 10^{-2} and 10^2 . Integration is carried out over a time period of $t = \max(100/\dot{\gamma}_0, 20\pi/\omega)$, using an integration time step of $\Delta t = \min(0.01/\dot{\gamma}_0, 0.02\pi/\omega)$. The initial conditions for the microstructure are isotropic, $\mathbf{a} = \delta/3$, and the microstructure parameter is $\beta = 6$. Upon starting the simulation, the signals of \mathbf{a} and Σ pass through a transient before reaching periodicity. The following results correspond to the periodic state.

Figure 4 shows the time-dependent components of the microstructure \mathbf{a} [Figs. 4(a) and 4(b)] and the particle stress Σ [Figs. 4(c) and 4(d)] for a large strain amplitude, $\gamma_0 = 10^2$ [Figs. 4(a) and 4(c)], and for a small strain amplitude, $\gamma_0 = 10^{-2}$ [Figs. 4(b) and 4(d)]. For the large strain amplitude, $\gamma_0 = 10^2$, the microstructure transitions between two steady states, with a positive and a negative shear direction, respectively. These steady states correspond to the horizontal segments of the time signals of \mathbf{a} in Fig. 4(a). In these steady phases, the particle stress Σ [Fig. 4(c)] is proportional to the oscillating shear rate $\dot{\gamma}$, and the second, relative normal stress difference is identical to that in steady shear flow, i.e., $\zeta_2 \approx -0.4$ (Fig. 2). For the small strain amplitude, $\gamma_0 = 10^{-2}$, the microstructure is isotropic with negligible oscillations [Fig. 4(b)], and the corresponding particle stress is Newtonian, i.e., without normal stresses [Fig. 4(d)].

Figure 5 shows the dynamic viscosity η_0 :

$$\eta_0 = \frac{\int_0^T \Sigma_{12}(t) \dot{\gamma}(t) dt}{\int_0^T \dot{\gamma}^2(t) dt}, \quad (17)$$

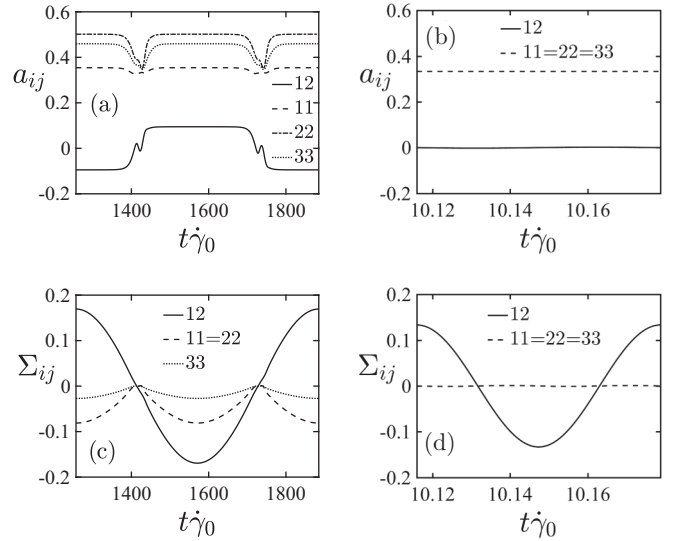


FIG. 4. Modeled [Eq. (12)] time-dependent components of the microstructure \mathbf{a} (a, b) and the particle stress Σ (c, d) in oscillating shear flow, with a strain amplitude of $\gamma_0 = \dot{\gamma}_0/\omega = 10^2$ (a, c) and 10^{-2} (b, d), using $\beta = 6$.

as a function of the strain amplitude γ_0 . The subscript 0 denotes an oscillation amplitude, and $T = 2\pi/\omega$ is the oscillation period. It is seen that the computed η_0 is an increasing function of γ_0 . This is due to the progressive alignment of \mathbf{a} with the compressive axis of the rate of strain tensor.

In Fig. 5 we also plot experimental data from Refs. [16,18], both at a volume fraction of $\phi = 0.4$. By using Eq. (15a), and by assuming a maximum packing fraction of $\phi_m = 0.6$, these conditions correspond to $\beta = 6$, which is the value used in the computations of Fig. 5. For $\gamma_0 \lesssim 10^{-1}$, both Eq. (12) and the experiments predict $\eta_0/\eta_{\infty} \approx 0.8$. This agreement supports the significance of Eq. (12) in describing the qualitative dynamics of the microstructure and stress, which is mainly attributed to the pair association and dissociation β -term.

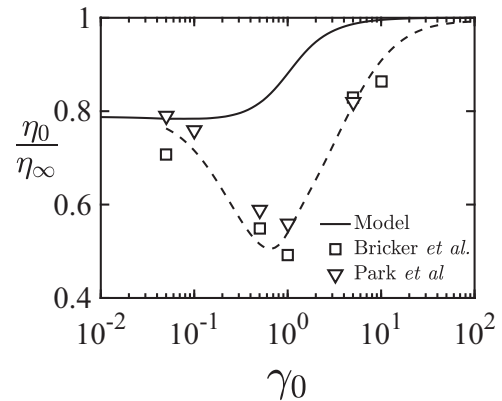


FIG. 5. Dynamic particle viscosity [Eq. (17)] in oscillating shear flow, scaled with the steady value, as a function of the strain amplitude. Comparison between model [Eq. (12)] using $\beta = 6$ (solid line), and experimental data from Ref. [16] (squares) and from Ref. [18] (triangles), both using $\phi = 0.4$. The dashed line is drawn to guide the eye.

There are quantitative differences, however. Equation (12) predicts a monotonic increase in $\eta_0/\eta_\infty(\gamma_0)$, while the experiments show nonmonotonic behavior, with a minimum of $\eta_0/\eta_\infty \approx 0.5$ at $\gamma_0 \sim 1$. The physical origin for this minimum is unclear and may be related to physical particle contacts, which are neglected in the model.

C. Oscillating normal stress

In suspension shear flow, nonzero normal stress differences are due to an anisotropic microstructure, and in oscillating shear flow, the microstructure anisotropy is controlled by the strain amplitude; see Fig. 4. Reference [17] quantified this effect experimentally, by measuring the migration of particles in an oscillating shear flow. This so-called ‘‘shear-induced migration’’ phenomenon is driven by the normal stresses; see, e.g., Ref. [40]. In their setup, the suspension resides in the gap, of width H , between two disks of radius R , one of which is rotating with an oscillating, angular frequency $\Omega(t)$, and one of which is stationary. In the limit of a negligible Reynolds number: $\Omega RH/\nu \ll 1$, the flow field is purely azimuthal: $U_\theta = r\Omega z/H$, and for small gaps, $H/R \ll 1$, the flow topology in each point corresponds to a simple shear, where the (θ, z, r) coordinates correspond to the flow direction, the gradient direction, and the vorticity direction, respectively. We model the particle migration velocity amplitude v_0 , that is induced by the stress amplitude Σ_0 , using the well-known suspension balance model (see, e.g., Ref. [40]):

$$v_0 = \frac{4\pi a^2(1-\phi)}{3\eta\phi C_1} \nabla \cdot \Sigma_0. \quad (18)$$

It is recalled that the subscript $_0$ denotes that the variable is an oscillation amplitude, and C_1 is the particle drag coefficient in a particle swarm, which is modeled using Eq. (4). Using that $\partial_z \Sigma_0 = \partial_\theta \Sigma_0 = \mathbf{0}$, the radial, polar coordinate component of the stress divergence reads

$$(\nabla \cdot \Sigma_0)_r = \partial_r \Sigma_{rr,0} + \frac{\Sigma_{rr,0} - \Sigma_{\theta\theta,0}}{r}. \quad (19)$$

By approximating $\partial_r \Sigma_{rr,0} \approx \Sigma_{rr,0}/r$, and by combining Eqs. (4), (18), and (19), we find

$$v_{r,0} = \frac{2a^2(1-\phi)^4}{9r\eta\phi} (2\Sigma_{rr,0} - \Sigma_{\theta\theta,0}).$$

To clarify this relation, we normalize the (dynamic) normal stress components by the steady shear stress, $\Sigma_{12,\infty} = \zeta_0\eta\dot{\gamma}_0$, where the relative particle shear viscosity ζ_0 is modeled using Eq. (13a), giving

$$v_{r,0} = \frac{2a^2\dot{\gamma}_0(1-\phi)^4}{9r\phi(1-\frac{\phi}{\phi_m})^2} \frac{2\Sigma_{rr,0} - \Sigma_{\theta\theta,0}}{\Sigma_{12,\infty}}.$$

The radial particle displacement per oscillation cycle, $\delta r = \int_0^T v_{r,0} dt$, is then found to be

$$\frac{r\delta r}{a^2\gamma_0} = \frac{4\pi(1-\phi)^4}{9\phi(1-\frac{\phi}{\phi_m})^2} \frac{\int_0^T (2\Sigma_{rr,0} - \Sigma_{\theta\theta,0}) \frac{dt}{T}}{\Sigma_{12,\infty}}, \quad (20)$$

where we have used that $\dot{\gamma}_0 T = 2\pi\gamma_0$.

Figure 6 shows the experimentally measured, scaled particle displacement $r\delta r/(a^2\gamma_0)$ versus the strain amplitude

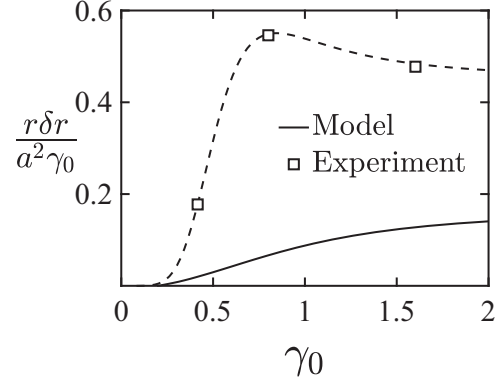


FIG. 6. Shear-induced migration per oscillation cycle δr , scaled with radial position r , particle radius a , and strain amplitude γ_0 . Comparison between model [Eqs. (12, 20)] using $\beta = 6$ (solid line) and experimental data from Ref. [17], using a volume fraction of $\phi = 0.4$ (markers). The dashed line is drawn to guide the eye.

γ_0 , using a volume fraction of $\phi = 0.4$ and an oscillation frequency of 1 s^{-1} [17]. In Fig. 6 we also plot the computed $r\delta r/(a^2\gamma_0)$, where we have used $\phi = 0.4$ and $\phi_m = 0.6$, which according to Eq. (15a) corresponds to $\beta = 6$, and a prefactor in Eq. (20) of $4\pi(1-\phi)^4/[9\phi(1-\phi/\phi_m)^2] \approx 1.8$. The model predictions are smaller, but of the same order of magnitude, as the experimental findings, and the qualitative trends are similar, with an initial increase and a subsequent plateau in $r\delta r/(a^2\gamma_0)$ as a function of γ_0 .

V. CONCLUSIONS

We have developed a model for the dynamics of the microstructure and the stress in dense suspensions of particles that interact purely via hydrodynamic forces. The model is derived from the Smoluchowski equation, which governs the distribution function of the separation vector between particle pairs.

Our main contribution is the formulation of the β -term in Eq. (12b), which accounts for the association and the dissociation of interacting particle pairs. With this term, the model captures the quantitatively correct tensorial behavior in steady shear flow and the qualitatively correct behavior in time-dependent flows.

Quantitative differences between model and experiment may point to the importance of physical contacts between the particles in the experiments, which are neglected in the model. It is noted that quantitative predictions may be improved by extending the model with additional terms to account for physical contacts. This, however, is beyond the scope of the present paper, which, instead of making accurate, quantitative predictions, is focused on gaining insight into the microstructural dynamics underlying the non-Newtonian behavior of particle suspensions.

ACKNOWLEDGMENT

We would like to acknowledge financial support from the Engineering and Physical Sciences Research Council in the United Kingdom, Grant No. EP/N024915/1.

- [1] E. Brown, N. A. Forman, C. S. Orellana, H. Zhang, B. W. Maynor, D. E. Betts, J. M. DeSimone, and H. M. Jaeger, Generality of shear thickening in dense suspensions, *Nat. Mater.* **9**, 220 (2010).
- [2] M. Wyart and M. E. Cates, Discontinuous Shear Thickening Without Inertia in Dense Non-Brownian Suspensions, *Phys. Rev. Lett.* **112**, 098302 (2014).
- [3] B. M. Guy, M. Hermes, and W. C. K. Poon, Towards a Unified Description of the Rheology of Hard-Particle Suspensions, *Phys. Rev. Lett.* **115**, 088304 (2015).
- [4] J. Comtet, G. Chatté, A. Niguès, L. Bocquet, A. Siria, and A. Colin, Pairwise frictional profile between particles determines discontinuous shear thickening transition in non-colloidal suspensions, *Nat. Commun.* **8**, 15633 (2017).
- [5] A. Singh and P. R. Nott, Experimental measurements of the normal stresses in sheared Stokesian suspensions, *J. Fluid Mech.* **490**, 293 (2003).
- [6] I. E. Zarraga, D. A. Hill, and D. T. Leighton Jr, The characterization of the total stress of concentrated suspensions of noncolloidal spheres in Newtonian fluids, *J. Rheol.* **44**, 185 (2000).
- [7] É. Couturier, F. Boyer, O. Pouliquen, and É. Guazzelli, Suspensions in a tilted trough: Second normal stress difference, *J. Fluid Mech.* **686**, 26 (2011).
- [8] T. Dbouk, L. Lobry, and E. Lemaire, Normal stresses in concentrated non-Brownian suspensions, *J. Fluid Mech.* **715**, 239 (2013).
- [9] F. Gadala-Maria and A. Acrivos, Shear-induced structure in a concentrated suspension of solid spheres, *J. Rheol.* **24**, 799 (1980).
- [10] V. G. Kolli, E. J. Pollauf, and F. Gadala-Maria, Transient normal stress response in a concentrated suspension of spherical particles, *J. Rheol.* **46**, 321 (2002).
- [11] T. Narumi, H. See, Y. Honma, T. Hasegawa, T. Takahashi, and N. Phan-Thien, Transient response of concentrated suspensions after shear reversal, *J. Rheol.* **46**, 295 (2002).
- [12] F. Blanc, F. Peters, and E. Lemaire, Local transient rheological behavior of concentrated suspensions, *J. Rheol.* **55**, 835 (2011).
- [13] N. Y. C. Lin, B. M. Guy, M. Hermes, C. Ness, J. Sun, W. C. K. Poon, and I. Cohen, Hydrodynamic and Contact Contributions to Continuous Shear Thickening in Colloidal Suspensions, *Phys. Rev. Lett.* **115**, 228304 (2015).
- [14] V. Breedveld, D. van den Ende, R. Jongschaap, and J. Mellema, Shear-induced diffusion and rheology of noncolloidal suspensions: Time scales and particle displacements, *J. Chem Phys.* **114**, 5923 (2001).
- [15] D. J. Pine, J. P. Gollub, J. F. Brady, and A. M. Leshansky, Chaos and threshold for irreversibility in sheared suspensions, *Nature (London)* **438**, 997 (2005).
- [16] J. M. Bricker and J. E. Butler, Oscillatory shear of suspensions of noncolloidal particles, *J. Rheol.* **50**, 711 (2006).
- [17] K. V. Deshpande and N. C. Shapley, Particle migration in oscillatory torsional flows of concentrated suspensions, *J. Rheol.* **54**, 663 (2010).
- [18] H.-O. Park, J. M. Bricker, M. J. Roy, and J. E. Butler, Rheology of oscillating suspensions of noncolloidal spheres at small and large accumulated strains, *Phys. Fluids* **23**, 013302 (2011).
- [19] N. Phan-Thien, X.-J. Fan, and B. C. Khoo, A new constitutive model for monodispersed suspensions of spheres at high concentrations, *Rheol. Acta* **38**, 297 (1999).
- [20] J. D. Goddard, A dissipative anisotropic fluid model for non-colloidal particle dispersions, *J. Fluid Mech.* **568**, 1 (2006).
- [21] J. J. Stickel, R. J. Phillips, and R. L. Powell, Application of a constitutive model for particulate suspensions: Time-dependent viscometric flows, *J. Rheol.* **51**, 1271 (2007).
- [22] R. N. Chacko, R. Mari, S. M. Fielding, and M. E. Cates, Shear reversal in dense suspensions: The challenge to fabric evolution models from simulation data, *J. Fluid Mech.* **847**, 700 (2017).
- [23] G. K. Batchelor, The stress system in a suspension of force-free particles, *J. Fluid Mech.* **41**, 545 (1970).
- [24] A. Einstein, Eine neue Bestimmung der Moleküldimensionen, *Ann. Phys.* **324**, 289 (1906).
- [25] J. F. Brady and G. Bossis, Stokesian dynamics, *Ann. Rev. Fluid Mech.* **20**, 111 (1988).
- [26] E. Lorenz, V. Sivadasan, D. Bonn, and A. G. Hoekstra, Combined Lattice—Boltzmann and rigid-body method for simulations of shear-thickening dense suspensions of hard particles, *Computers Fluids* **172**, 474 (2018).
- [27] J. D. Goddard, An elasto-hydrodynamic theory for the rheology of concentrated suspensions of deformable particles, *J. Non-Newtonian Fluid Mech.* **2**, 169 (1977).
- [28] B. H. A. A. Van den Brule and R. J. J. Jongschaap, Modeling of concentrated suspensions, *J. Stat. Phys.* **62**, 1225 (1991).
- [29] N. Phan-Thien, Constitutive equation for concentrated suspensions in Newtonian liquids, *J. Rheol.* **39**, 679 (1995).
- [30] R. C. Ball and J. R. Melrose, A simulation technique for many spheres in quasi-static motion under frame-invariant pair drag and Brownian forces, *Physica A* **247**, 444 (1997).
- [31] M. Doi and S. F. Edwards, *The Theory of Polymer Dynamics* (Oxford University Press, Oxford, 1988).
- [32] J. F. Richardson and W. N. Zaki, Sedimentation and fluidisation: Part I, *Trans. Inst. Chem. Eng.* **32**, S82 (1954).
- [33] S. Kim and S. Karilla, *Microhydrodynamics* (Butterworth-Heinemann, London, 1991).
- [34] S. G. Advani and C. L. Tucker III, Closure approximations for three-dimensional structure tensors, *J. Rheol.* **34**, 367 (1990).
- [35] E. J. Hinch and L. G. Leal, Constitutive equations in suspension mechanics. Part 2. Approximate forms for a suspension of rigid particles affected by Brownian rotations, *J. Fluid Mech.* **76**, 187 (1976).
- [36] I. M. Krieger, Rheology of monodisperse latices, *Adv. Colloid. Interfac.* **3**, 111 (1972).
- [37] D. Lootens, H. Van Damme, Y. Hémar, and P. Hébraud, Dilatant Flow of Concentrated Suspensions of Rough Particles, *Phys. Rev. Lett.* **95**, 268302 (2005).
- [38] J. R. Royer, D. L. Blair, and S. D. Hudson, Rheological Signature of Frictional Interactions in Shear Thickening Suspensions, *Phys. Rev. Lett.* **116**, 188301 (2016).
- [39] L. C. Hsiao, S. Jamali, E. Glynos, P. F. Green, R. G. Larson, and M. J. Solomon, Rheological State Diagrams for Rough Colloids in Shear Flow, *Phys. Rev. Lett.* **119**, 158001 (2017).
- [40] P. R. Nott, E. Guazzelli, and O. Pouliquen, The suspension balance model revisited, *Phys. Fluids* **23**, 043304 (2011).